

Overview of Physics Results from MAST

H Meyer¹, R J Akers¹, F Alladio², L C Appel¹, K B Axon¹, N Ben Ayed³, P Boerner¹¹, R J Buttery¹, P G Carolan¹, D Ciric¹, C D Challis¹, I T Chapman¹, G Coyler¹, J W Connor¹, N J Conway¹, S Cowley¹, M Cox¹, G F Counsell¹, G Cunningham¹, A Darke¹, M deBock¹, G deTemmerman¹, R O Dendy¹, J Dowling¹, A Yu Dnestrovskij⁴, Yu N Dnestrovskij⁴, B Dudson³, D Dunai⁵, M Dunstan¹, A R Field¹, A Foster⁶, L Garzotti¹, K Gibson³, M P Gryaznevich¹, W Guttenfelder⁷, N C Hawkes¹, J Harrison³, P Helander⁸, T C Hender¹, B Hnat⁷, M J Hole⁹, D F Howell¹, M Duc Hua¹⁰, A Hubbard¹¹, M Istenic¹, N Joiner¹⁰, D Keeling¹, A Kirk¹, H R Koslowski¹², Y Liang¹², M Lilley¹⁰, S Lisgo¹, B Lloyd¹, G P Maddison¹, R Maingi¹⁴, A Mancuso², S J Manhood¹, R Martin¹, G J McArdle¹, J McCone¹⁵, C Michael¹, P Micozzi², T Morgan³, A W Morris¹, D G Muir¹, E Nardon¹, G Naylor¹, M R O'Brien¹, T O'Gorman¹⁵, A Patel¹, S D Pinches¹, J Preinhaelter¹⁶, M N Price¹, E Rachlew¹⁶, D Reiter¹², C M Roach¹, V Rozhansky¹⁷, S Saarelma¹, A Saveliev¹⁸, R Scannell¹, S E Sharapov¹, V Shevchenko¹, S Shibaev¹, H Smith¹⁰, G E Staebler¹⁹, D Stork¹, J Storrs¹, A Sykes¹, S Tallents¹⁰, P Tamain¹, D Taylor¹, D Temple¹⁰, N Thomas-Davies¹, A Thornton³, A. Thyagaraja¹, M R Turnyanskiy¹, J Urban¹⁶, M Valovic¹, R G L Vann³, F Volpe¹, G Voss¹, M J Walsh¹, S E V Warder¹, R Watkins¹, H R Wilson³, M Windridge¹⁰, M Wisse¹, A Zabolotski¹, S Zoletnik⁴, O Zolotukhin¹ and the MAST and NBI teams

¹EURATOM/UKAEA Fusion Association, Culham Science Centre, Abingdon, UK.

²Associazione EURATOM-ENEA sulla Fusione, Frascati, Rome, Italy.

³University of York, Heslington, York, UK.

⁴Russian Research Centre, Kurchatov Institute, Institute of Nuclear Fusion, Moscow, Russia.

⁵KFKI-RMKI, Association EURATOM, Pf. 49, H-1525 Budapest, Hungary

⁶University of Strathclyde, Glasgow, UK.

⁷Department of Physics, Warwick University, UK.

⁸Max-Planck-Institute for Plasma Physics, Greifswald, Germany.

⁹Department of Theoretical Physics, Research School of Phys. Sci. & Eng. Australian National University Canberra ACT 0200, Australia

¹⁰Imperial College of Science, Technology and Medicine, London, UK.

¹¹MIT Plasma Science and Fusion Centre, Cambridge, MA 02139, USA.

¹² Forschungszentrum Jülich GmbH, Association EURATOM-FZ Jülich, Institut für Plasmaphysik, Trilateral Euregio Cluster, D-52425 Jülich, Germany

¹³Dept. of Physics, KTH, EURATOM -VR Association, Stockholm, Sweden.

¹⁴Oak Ridge National Laboratory, Oak Ridge, USA.

¹⁵University College, Cork, Association EURATOM-DCU Ireland.

¹⁶EURATOM/IPP.CR Fusion Association, Prague, Czech Republic.

¹⁷St. Petersburg State Polytechnical University, St. Petersburg, Russia.

¹⁸Ioffe Institute, Politekhnicheskaya 26, 194021 St. Petersburg, Russia.

¹⁹General Atomics, P.O. Box 85608, San Diego, California 92186-5608, USA.

E-mail: Hendrik.Meyer@ukaea.org.uk

PACS numbers: 52.55.Fa, 52.25.Xz, 52.35.Ra

Abstract. Several improvements to the MAST plant and diagnostics have facilitated new studies advancing the physics basis for ITER and DEMO, as well as for future spherical tokamaks. Using the increased heating capabilities $P_{\text{NBI}} \leq 3.8$ MW H-mode at $I_p = 1.2$ MA was accessed showing that the energy confinement on MAST scales more weakly with I_p and more strongly with B_t than in the ITER IPB98(y,2) scaling. Measurements of the fuel retention of shallow pellets extrapolate to an ITER particle throughput of 70% of its original designed total throughput capacity. The anomalous momentum diffusion, χ_ϕ , is linked to the ion diffusion, χ_i , with a Prandtl number close to $P_\phi \approx \chi_\phi/\chi_i \approx 1$, although χ_i approaches neoclassical values. New high spatial resolution measurements of the edge radial electric field, E_r , show that the position of steepest gradients in electron pressure and E_r (i.e. shearing rate) are coincident, but their magnitudes are not linked. The T_e pedestal width on MAST scales with $\sqrt{\beta_{\text{pol}}^{\text{ped}}}$ rather than ρ_{pol} . The ELM frequency for type-IV ELMs, new in MAST, was almost doubled using $n = 2$ resonant magnetic perturbations from a set of 4 external coils ($n = 1, 2$). A new internal 12 coil set ($n \leq 3$) has been commissioned. The filaments in the inter-ELM and L-mode phase are different from ELM filaments, and the characteristics in L-mode agree well with turbulence calculations. A variety of fast particle driven instabilities were studied from 10 kHz saturated fishbone like activity up to 3.8 MHz compressional Alfvén eigenmodes (CAE). Fast particle instabilities also affect the off-axis NBI current drive, leading to fast ion diffusion of the order of 0.5 m²/s and a reduction of the driven current fraction from 40% to 30%. EBW current drive start-up is demonstrated for the first time in a spherical tokamak generating plasma currents up to 55 kA. Many of these studies contributed to the physics basis of a planned upgrade to MAST.

1. Introduction:

MAST [1] is one of the two leading tight aspect ratio ($A = \varepsilon^{-1} = R/a = 0.85$ m/0.65 m \sim 1.3, $I_p \leq 1.5$ MA) tokamaks in the world. The hot $T \leq 3$ keV, dense $n_e = (0.1 - 1) \times 10^{20}$ m⁻³ and highly shaped ($\delta \leq 0.5$, $1.6 \leq \kappa \leq 2.5$) plasmas are accessed at moderate toroidal field $B_t(R = 0.7$ m) ≤ 0.62 T and show many similarities to conventional aspect ratio tokamaks. Detailed physics studies using the extensive array of state of the art diagnostics and access to different physics regimes help to consolidate the physics basis for ITER and DEMO [2, 3], and explore the viability of future devices based on the spherical tokamak (ST) concept such as a component test facility (CTF) [4] or an advanced power plant [5]. The challenge for today's experiments is to find an integrated scenario that extrapolates to these future devices, in particular to develop plasmas with reduced power load on plasma facing components, notably from edge localised modes (ELM), but high confinement facilitated by internal or edge transport barriers. For steady state tokamak operation non-inductive current drive techniques, including off-axis, have to be explored and a high bootstrap current fraction is needed. Fast particle instabilities, more prominent in

future devices due to the α -particles may affect the performance of advanced fusion plasmas by broadening the fast particle distribution or spawning more detrimental instabilities. On MAST studies of ELM and pedestal characteristics (Sec. 3) and scrape-off layer transport (Sec. 4) help to consolidate our understanding of the plasma edge. These investigations are done with and without resonant magnetic perturbations for ELM mitigation (Sec. 3.2) or in the presence of pellet fuelling (Sec. 3.4). Core transport and confinement (Sec. 5) are scrutinised by detailed modelling as well as scaling experiments. With its high fraction of super-Alfvénic particles, MAST is ideally suited to study the impact of fast particle driven instabilities (Sec. 6) on confinement, momentum transport (Sec. 5.3), off-axis current drive (Sec. 7.2), and develop general understanding of fast particle instabilities. More specific for the ST is the development of non-inductive start-up using electron Bernstein waves (EBW, Sec. 7.1). Many of the studies benefited from the enhanced plant and diagnostic capabilities (Sec. 2), and have contributed to an extensive physics basis for a planned upgrade to MAST (Sec. 8)

2. Diagnostic and Plant improvements:

During the last two years MAST had major plant improvements. The neutral beam heating power was upgraded to $P_{\text{NBI}} \leq 3.8$ MW by replacing one Duopigatron source ($P_{\text{NBI}} \leq 1.7$ MW, $\Delta t \leq 0.4$ s) with a JET style PINI injector ($P_{\text{NBI}} \leq 2.5$ MW, $\Delta t \leq 5$ s). A similar upgrade is underway for the second beam line. A new toroidal array of 12 internal four turn coils (6 above, and 6 below the mid-plane every 60°) with 2 sets of power supplies enabling low current $I_{\text{TAE}}^{\text{AC}} \leq 4$ A AC operation up-to 500 kHz (TAE), and high current $I_{\text{RMP}}^{\text{DC}} \leq 1.4$ kA DC operation in each coil (RMP). These coils are used for TAE excitation (Sec. 6) and ELM mitigation (Sec. 3.2) studies. The error field correction coils (EFC) have been equipped with new power supplies similar to the DC power supplies of the internal coils freeing 2 fast amplifiers ($f \leq 1$ kHz) to improve the vertical feedback control. A $\Delta t \leq 90$ ms $P_{\text{RF}} \leq 0.1$ MW 28 GHz gyrotron for start-up studies has also been commissioned (Sec. 7.1).

With respect to diagnostic enhancements the most notable are:

- the new 35 channel MSE system [6, 7] ($\Delta r \leq 2.5$ cm, $\Delta t \leq 5$ ms, pitch angle resolution $\Delta\alpha \leq 0.5^\circ$),
- the upgrade of the NdYAG based Thomson scattering (TS) system from a 200 Hz 4 laser system with $E_{\text{las}} \approx 0.9$ J to a 240 Hz 8 laser system with $E_{\text{las}} \approx 1.5$ J [8],
- the new 120 chord edge Doppler system [9],
- and the unique long wavelength IR camera $8.0 \mu\text{m} \leq \lambda \leq 10.5 \mu\text{m}$.

The improvement of the Thomson scattering system is part of an ongoing upgrade, which will bring the spatial resolution of the NdYAG system with 120 channels into the region of the ion Larmor radius $\rho_i \approx 1$ cm with a factor of two larger signal. These diagnostic improvements are augmented by a recently developed interactive, integrated analysis package (MC³) to improve the overall data consistency. A further major change is the upgrade of a large fraction of the data acquisition hardware to allow up to 5s sampling and up to 10 MHz sampling rate.

3. H-mode edge, ELM stability and fuelling:

3.1. ELMs and pedestal:

Using the NdYAG edge TS system on the low field side (LFS) [10] in conjunction with the high field side (HFS) data from the Ruby system earlier studies on the comparison of LFS and HFS pedestals with the Ruby system alone [11, 12] were revisited. The NdYAG edge system enables better LFS pedestal measurements than the Ruby system due to its capability to measure lower T_e and n_e . The study covered a wide data set with $0.5 \text{ MA} \leq I_p \leq 1.2 \text{ MA}$, $0.2 \leq n_e/n_G \leq 0.9$ (n_G : Greenwald density), $3 \leq q_{95} \leq 7$, $0.45 \text{ T} \leq B_t \leq 0.55 \text{ T}$, triangularity of $0.3 \leq \delta \leq 0.5$, elongation of $1.6 \leq \kappa \leq 2.1$ and auxiliary heating power of $1.0 \text{ MW} \leq P_{\text{NBI}} \leq 3.8 \text{ MW}$ in double null (DN) and single null (SN) configurations [13].

Of particular interest is the different behaviour of the density pedestal width, Δ_{n_e} , in DN and SN. In DN Δ_{n_e} is narrower in flux space on the HFS than on the LFS, but not so in SN [13]. In contrast, the temperature, Δ_{T_e} , and interestingly also the pressure, Δ_{p_e} , pedestal widths are similar in flux space on the HFS and LFS in both configurations. This has two major consequences in DN. Firstly, the electron pressure is not a flux function, and secondly, the HFS location for the n_e barrier and T_e barrier are not the same. In DN Δ_{n_e} is the same in real space on the HFS and the LFS showing the importance of the ionisation source for the density pedestal formation. This may be explained by the fact that the scrape-off-layer (SOL) on the HFS is much narrower in DN than in SN [14].

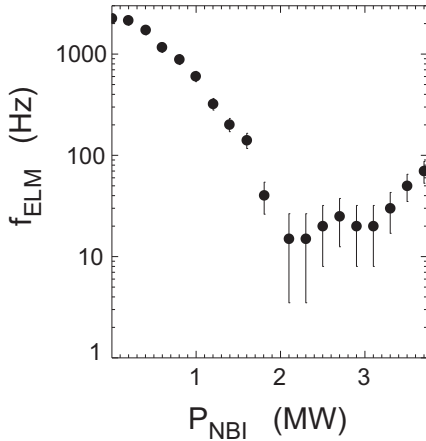


Figure 1. Variation of ELM repetition rate with NBI power.

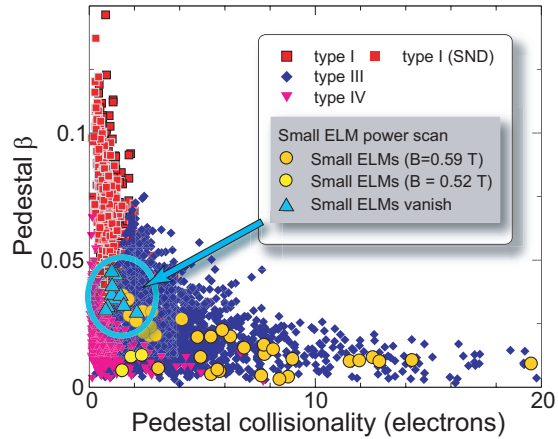
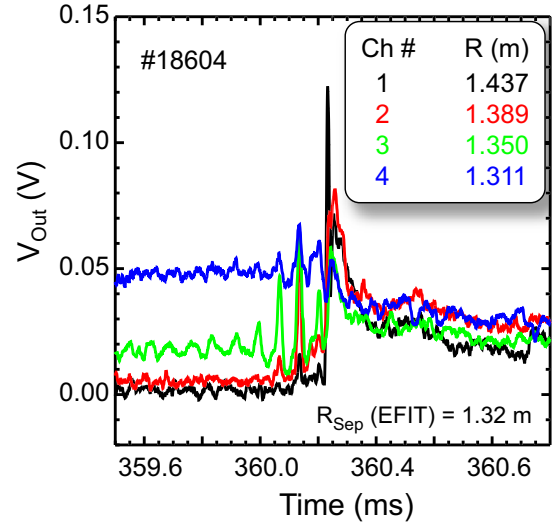


Figure 2. Existence space of different ELM types with respect to electron β and ν^* at the top of the pedestal.

Three different large ELM types can be distinguished in this data set: ELMs at high edge collisionality ($T_e^{\text{ped}} \lesssim 0.15 \text{ keV}$, $n_e^{\text{ped}} \gtrsim 2 \times 10^{19} \text{ m}^{-3}$) where the repetition rate decreases with increasing power (type-III); ELMs at lower edge collisionality ($T_e^{\text{ped}} \gtrsim 150 \text{ eV}$, $n_e^{\text{ped}} \gtrsim 2.5 \times 10^{19} \text{ m}^{-3}$), but high density where the repetition rate slowly increases with power (type-I, Fig. 1); ELMs at low collisionality and low density ($T_e^{\text{ped}} \gtrsim 100 \text{ eV}$, $n_e^{\text{ped}} \lesssim 2.5 \times 10^{19} \text{ m}^{-3}$) with characteristics of type-IV ELMs (or the low collisionality branch of type-III ELMs). In

addition a type of small ELMs with $n \sim 30$ co-current rotating filaments and distinct regular mode structure has been observed. Only a few of these filaments detach. At high pedestal pressure approaching the type-I ELM regime, the small ELMs vanish (Fig. 2). A comparison to small ELMs in NSTX and Alcator C-MOD [15] shows that these ELMs are distinct from the small type-V ELMs observed on NSTX [16], because of the different mode structure and rotation direction.

Figure 3. BES signal at the plasma edge during a type-I ELM.



In SN only type-I ELMs have been observed [13], although the edge stability is not changed by the configuration [12]. These type-I ELMs are sometimes preceded by a precursor as can be seen from Fig. 3 showing data from a trial 8 channel beam emission spectroscopy (BES) system. This burst of edge localised fluctuations is locked in frequency to a steady core $n = 1$ MHD mode (Sec. 6). For type-I ELMs the ideal edge stability analysis performed is consistent with the peeling-ballooning theory for ELM triggering [17, 18]. The profiles just prior to a type-I ELM are close to the peeling-ballooning stability boundary, whereas those for the type-III and type-IV ELMs are in the ideal MHD stable region and are assumed to be driven by resistive modes.

The type-IV ELM regime as well as the data from different magnetic configurations help to shed light on the pedestal width scaling with respect to the co-linearity between the normalised poloidal Larmor radius ρ_{pol}^* and β_{pol} . From the picture of turbulence suppression by $E \times B$ flow shear one would expect the pressure pedestal width to change like $\Delta_p/a = 2\sqrt{6\varepsilon/(1+\varepsilon)}\rho_{\text{pol}}^*$. On MAST, however, very little change of Δ_{T_e} is observed with respect to ρ_{pol}^* , but Δ_{T_e} clearly increases with $\beta_{\text{pol}}^{\text{ped}}$ in suitable comparison discharges. This is similar to the recent findings of $\Delta_p/a \propto (\rho_{\text{pol}}^*)^{0.1}\beta_{\text{pol}}^{0.5}$ on JT60-U using deuterium and hydrogen discharges [19]. From the full data set one gets a scaling $\Delta_{T_e}/a \propto \beta_{\text{pol}}^\alpha$ with $\alpha_{\text{DN}} = 0.52 \pm 0.03$ and $\alpha_{\text{SN}} = 0.47 \pm 0.05$ in DN and SN respectively neglecting the ρ_{pol}^* dependence.

3.2. ELM mitigation:

For studies of ELM mitigation by resonant magnetic perturbations MAST is now equipped with two coil sets: The new *internal* (RMP) coil set (Sec. 2) similar to the DIII-D I-coils [20], and the *external* error field correction coil set (EFC) with four three turn coils ($I_{\text{EFC}} \leq 5$ kA each) each 90° toroidal extent and ~ 4 m high on the vessel. This set-up gives flexibility in the toroidal mode spectrum $n \leq 3$ and phasing, with the poloidal spectrum determined by the pitch angle and the current parity of the upper and lower internal coils [21].

Figure 4. Chirikov parameter as function of normalised radius for DIII-D \diamond , JET \square , MAST \times (EFC $n = 2$), \circ (EFC $n = 1$), \star (RMP $n = 3$).

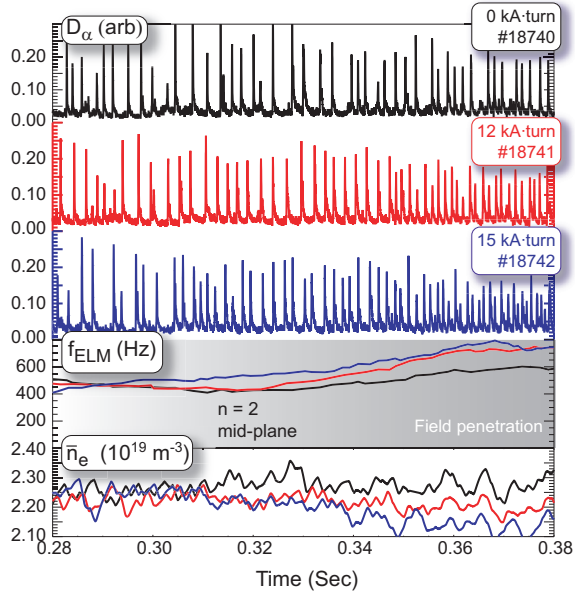
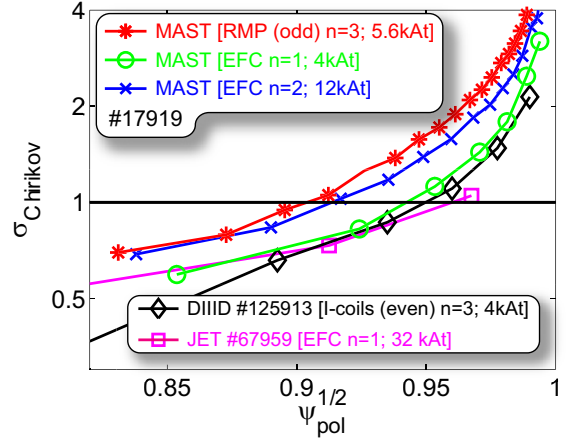


Figure 5. Mitigation of type-IV ELMs using the $n = 2$ perturbation produced by the external EFC coils. Shown are the D_α intensity, ELM frequency and line averaged density for increasing coil current from black to red to blue.

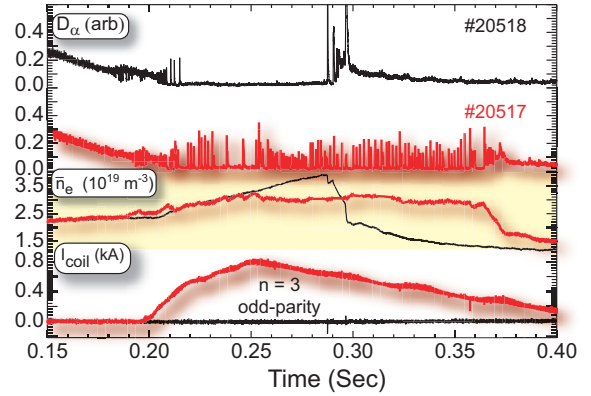


Figure 6. Effect of the $n = 3$ perturbation produced by the internal RMP coils (red) on a naturally ELM-free H-mode (black). Shown are D_α intensity, line averaged density, and the coil current in the RMP coils.

With an $n = 1$ perturbation from the *EFC* coil set, in a similar way to the recent JET studies [22], locked modes were triggered before ELMs were affected, although on

MAST a higher Chirikov parameter σ_{Chirikov} [23, 24] calculated in vacuum approximation is achieved by the coils (Fig. 4) with coil currents well below the locked mode threshold [25]. The Chirikov parameter measures the island overlapping and $\sigma_{\text{Chirikov}} > 1$ indicates edge ergodisation. In the $n = 2$ configuration an increase of the ELM frequency from the natural frequency of $f_{\text{ELM}} \approx 0.6$ kHz to $f_{\text{ELM}}^{\text{EFC}} \approx 1$ kHz has been observed in the low collisionality type IV ELM regime as can be seen from Fig. 5. Here, only one of the two coil pairs was connected to give an $n = 2$ perturbation and the other was used to cancel partly the intrinsic error field. Commissioning studies with the new *RMP* coil set in Ohmic discharges show a distinct density pump-out during the period when the q-profile is resonant to the perturbation. In this period there seems also to be a small change towards more positive E_r as expected for an ergodised edge. Initial experiments in H-mode showed that application of the coils in an originally ELM-free H-mode in DN configuration triggered type-III ELMs (Fig. 6). This is similar to results first observed on COMPASS-D [26, 27] and has also been seen on other devices. Here the current of initially $I_{\text{RMP}} = 0.8$ kA (3.2 kA · turns) had to be reduced in order to achieve a phase with regular ELMs.

3.3. Radial electric field:

The evolution and structure of the radial electric field, E_r , on MAST in L-mode and H-mode has been studied using edge Doppler spectroscopy [9]. E_r is derived from the radial force balance of the observed ion species (here He^+ at $\lambda_0 = 468.6$ nm). Using a local helium gas puff a spatial resolution of the E_r profile of $\Delta r = (3 - 6)$ mm is achieved with a typical time resolution of $\Delta t = 5$ ms on roughly 60 spatial points with a chord distance of 1.5 mm. The evolution of E_r through an L to H transition is shown in Fig. 7. In H-mode a narrow negative edge well evolves in E_r with a typical minimum of $E_r^{\text{min}} \approx -15$ kV/m.

In Fig. 8 the electron pressure gradient versus the electric field gradient calculated over the whole pedestal region is shown for two different H-mode discharges well into an ELM free phase. These discharges with different plasma current, $I_p = 0.7$ MA and $I_p = 1.1$ MA, and different fuelling were chosen because of their distinct difference in the width of the E_r well and the pedestal. The high current discharge has a much narrower E_r well, but a shallower pedestal pressure compared to the low current discharge. For both discharges clearly the strongest negative pressure gradient, ∇p_e is associated with the negative gradient in E_r . The magnitude of ∇p_e is not correlated with ∇E_r suggesting that physical processes other than the $E \times B$ flow shearing rate limit the ∇p_e [9].

3.4. Pellet fuelling:

Using an 8 barrel pellet injector the particle transport in MAST was studied with pneumatically accelerated pellets. Typical pellet speeds between $250 \text{ m/s} \leq v_{\text{pellet}} \leq 400 \text{ m/s}$ from the high field side (HFS) top of the machine result in shallow pellet injection between $0.6 \leq \rho_{\text{pel}} = \sqrt{\psi_{\text{N,pel}}} \leq 0.9$. The pellet trajectory has been observed using unfiltered high speed visible imaging as well as time averaged narrow band filtered visible imaging in a line free region at $\lambda = (523.44 \pm 0.32)$ nm to measure bremsstrahlung. These data are used

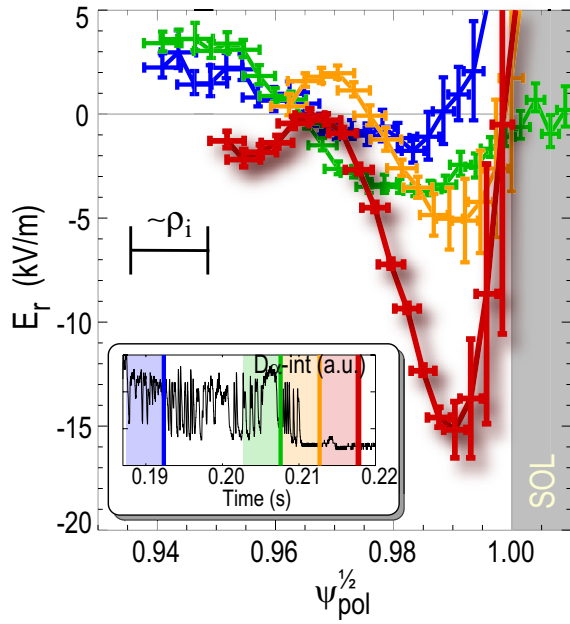


Figure 7. Evolution of the radial electric field through an L–H transition on MAST [9].

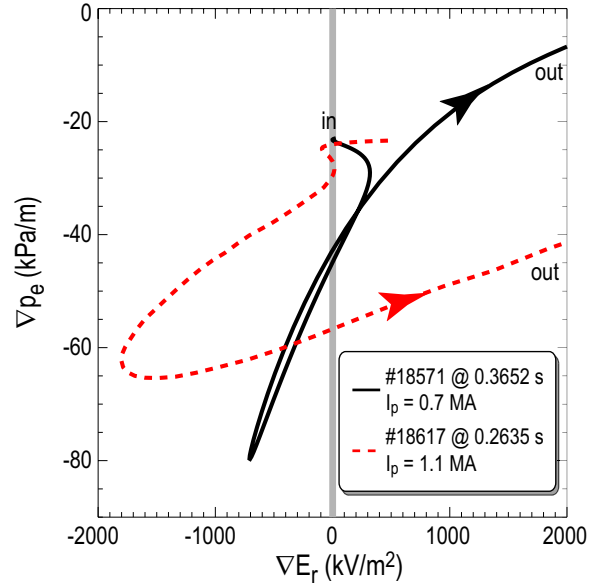


Figure 8. ∇p_e versus ∇E_r in the pedestal region for a low current (black, solid) and high current (red, dashed) H-mode (arrows indicate R) [9].

to establish the pellet deposition radius ρ_{pel} [28]. High resolution TS measurements with the single time Ruby system event triggered from the pellet system itself are used to determine the pellet retention time τ_{pel} [28, 29].

Fig. 9 shows that at ITER like deposition radius the retention time normalised to the energy confinement time in ELMy H-mode is only $\tau_{\text{pel}}/\tau_E = 0.2$. Hence the particle throughput estimated for ITER $\Phi_{\text{pel}} \approx n_e S(a - r_{\text{pel}})/\tau_{\text{pel}} \approx 70 \text{ Pam}^3/\text{s}$ is about 70% of the originally foreseen ITER design value, which would have left little headroom for other gas throughput from gas puffing or ELM-pacing pellets. Here nominal values are used for ITER [2] of $n_e = 10^{20} \text{ m}^{-3}$, plasma surface $S = 683 \text{ m}^2$ and $\tau_E = 3.7 \text{ s}$. Comparisons with predictive pellet ablation codes show that the ∇B -drift as well as the plasma pre-cooling due to the drift is needed in order to understand the post pellet n_e profiles on MAST. The mostly adiabatic response of the kinetic profiles to the perturbation by the pellet leads to a shorter T_e gradient length $L_{T_e} = T_e/(\nabla T_e)$ in the region of the positive density gradient. This leads to an increased turbulence level in this region according to calculations with the GS2 [30] and CUTIE [31] codes. This increased turbulence leads to an increased inwards particle flux which is needed to understand the pellet retention time [28]. As can be seen from the square in Fig. 9 the pellet retention time simulated with CUTIE by approximating the pellet particle source is in good agreement with the experiment.

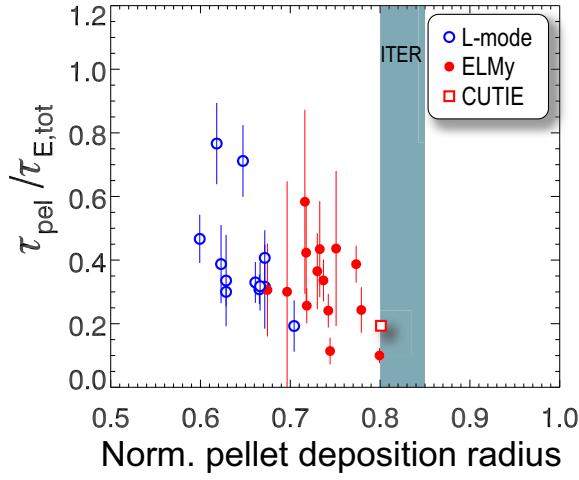


Figure 9. Pellet retention time normalised to τ_E as a function of pellet deposition radius for L-mode (blue open circles) and ELMy H-mode (red full circles) [28].

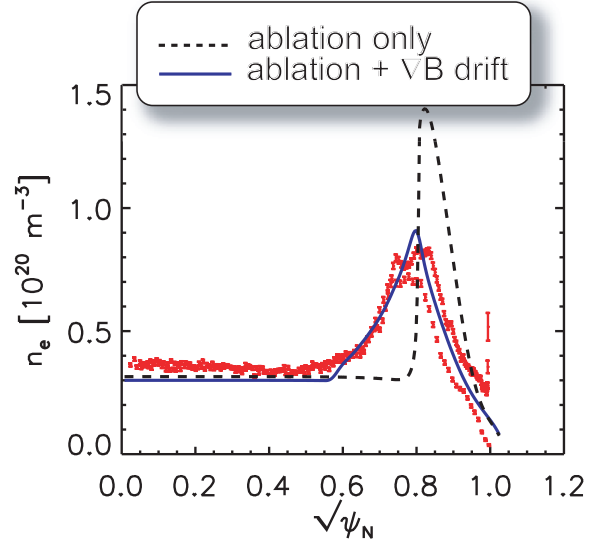


Figure 10. Comparison of measured density profile at the HFS and LFS side (red) with the predicted pellet deposition using the PELDEP2D code without (dashed line) and with (solid blue line) ∇B drift included [28].

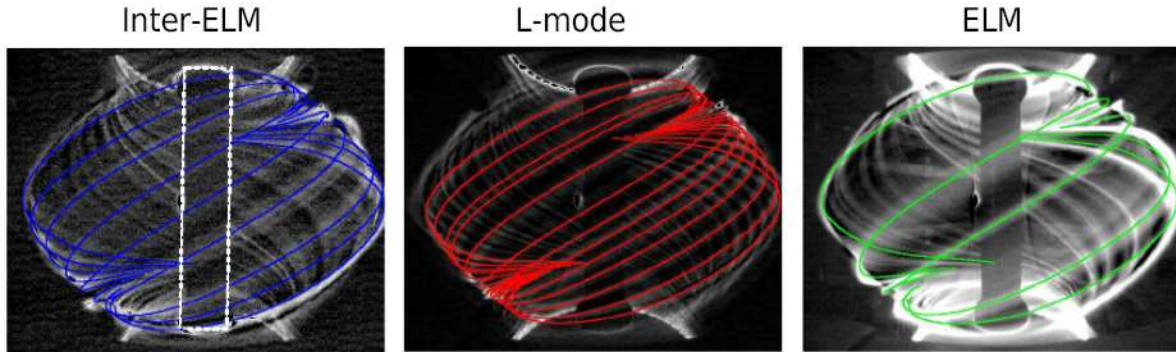


Figure 11. Filamentary structures in the inter ELM period (left), L-mode (middle) and during an ELM (right) with the magnetic field lines overlaid.

4. SOL modelling and Edge filaments:

In recent years much attention was devoted to ELM filaments [32–34] (Fig. 11 right), but it has been long known that the intermittent L-mode transport is also filamentary [35, 36] (Fig. 11 middle). Careful background subtraction shows that field-aligned filaments are also present in inter ELM periods [37] (Fig. 11 left). The characteristics of these filaments as deduced from the visible imaging are listed in Table 1 [38]. This comparison suggests that the sporadic inter-ELM filaments are more closely related to L-mode filaments than to ELM filaments (e.g. drift waves rather than ideal MHD). The L-mode turbulence was modelled using the BOUT code [39] in good agreement with the experimental data. It should be noted that the small ELMs described in Sec. 3.1 are different from the inter-ELM filaments with respect to their mode

Table 1. Filament properties from fast imaging and BOUT L-mode modelling (τ : life time, $v_{r,\phi}$: radial, toroidal velocity, N number of filaments, $L_{\text{rad},\theta}$: radial, poloidal scale length)

Regime	τ (μs)	v_r (km/s)	v_ϕ (km/s)	N	L_{rad} (cm)	L_θ (cm)
L-mode	40 - 60	0.5 - 1.5	2 - 9	20 - 50	5 - 10	7 - 9
Inter-ELM	50 - 120	1 - 2	3 - 12.5	10 - 40	3 - 5	9 - 12
ELM	100 - 180	1 \rightarrow 9	10 - 30	10 - 20	4 - 6	2 - 6
BOUT L-mode		~ 0.5		~ 40		~ 5

structure. In contrast to the inter-ELM filaments, the small ELM shows a very regular distinct mode structure in the visible imaging. Empirical modelling to include filamentary effects on SOL transport is underway [40].

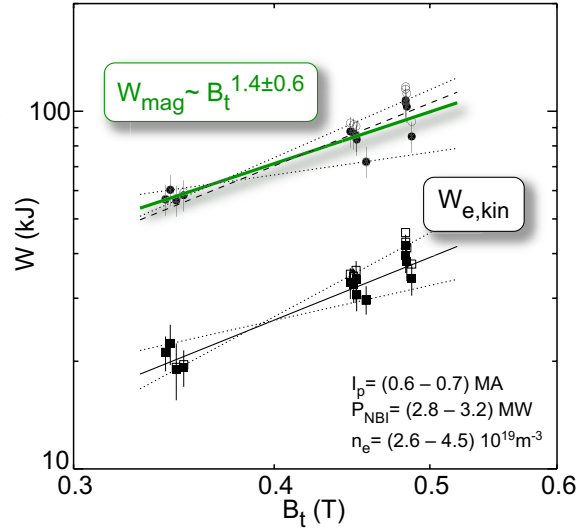
5. Core Confinement and Transport:

Transport in MAST is investigated using analytic theory and a variety of codes including gyrokinetic (flux-tube: GS2; global: ORB5, GYRO) and mesoscale MHD turbulence simulations, predictive modelling with reduced theoretical models, and interpretative modelling [41]. In many cases, the experimentally observed toroidal flow shear is sufficient to suppress long wavelength (ITG) turbulence. Predictive modelling of non sawtoothed L-mode discharges was done with GLF23, TGLF, and ORB5 [41, 42]. GLF23 and TGLF tend to underestimate the core transport ($r/a < 0.4$) with $E \times B$ shear stabilisation enabled (in particular for the electrons) and overestimate the ion transport without $E \times B$ shear. ORB5 without $E \times B$ shear underestimates core transport. TGLF predicts electron transport dominated by high-k (ETG) turbulence, but other mechanisms such as MHD or fast particle driven micro-tearing may also cause significant electron transport leading to the less peaked T_e and T_i profiles as observed and predicted by CUTIE (albeit for circular flux surfaces and zero particle trapping). The non linear CPTM model [43] has been used on H-mode discharges, giving reasonable agreement for n_e and T_e profiles.

5.1. Energy confinement scaling:

The MAST H-mode confinement scaling data base was expanded to higher plasma current $I_p \leq 1.2$ MA and higher heating powers $P_{\text{NBI}} \leq 3.8$ MW. Furthermore, dedicated scaling experiments with respect to the toroidal field B_t and I_p have been performed. An example of such a scan in case of B_t is shown in Fig. 12. The data now approach the $I_p/I_{\text{rod}} \approx 0.65$ of an ST-CTF design point [4] at stored energies of $W_{\text{mag}} = 150$ kJ. With respect to dimensionless parameters the MAST data set connects to CTF values in ρ_* , q_{eng} , and β_N but extrapolation with respect to ν_* is still more than an order of magnitude. In terms of engineering parameters the MAST data set as well as the dedicated scans support a slightly weaker scaling of τ_E , with I_p and a much stronger scaling with B_t than the IPB98(y,2) scaling [29]. This is in agreement with results from NSTX [44]. Depending on the scaling method the coefficients for I_p and B_t are $0.4 \leq \alpha_{I_p} \leq 0.6$ and $1.3 \leq \alpha_{B_t} \leq 1.6$ respectively compared to $\alpha_{I_p} = 0.93$

Figure 12. Two point magnetic field scan showing the strong scaling of confinement with B_t on MAST [29].



and $\alpha_{B_t} = 0.15$ for IPB98(y,2). Such a scaling extrapolates to $H_H = \tau_E/\tau_{scal.} \approx 1.6$ for a current ST-CTF design point compared the assumed $H_H = 1.3$. Transport analysis indicates that the different scaling of τ_E with I_p and B_t in ST's may arise from a dependence of the effective heat diffusivity of $\chi_{eff} \propto \chi_{GB} q^{\alpha_q} \nu_*^{\alpha_\nu}$ with $\alpha_q \lesssim 1$ and $\alpha_\nu \approx 3/4$ (χ_{GB} gyro-Bohm diffusivity). This is slightly weaker in q and stronger in ν_* than found in conventional tokamaks. It may well be that this different scaling is a manifestation of the dominant ETG turbulence as indicated by predictive modelling whilst ITG and TEM turbulence is largely suppressed.

5.2. Particle and impurity confinement:

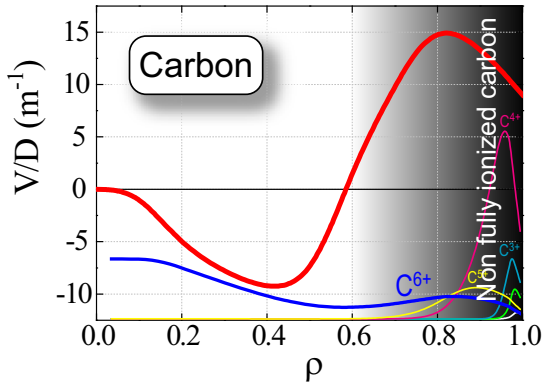


Figure 13. Modelled ratio of impurity pinch velocity and impurity diffusion coefficient for a MAST L-mode discharge using the STRAHL [45] code (also shown: profiles of ionisation states).

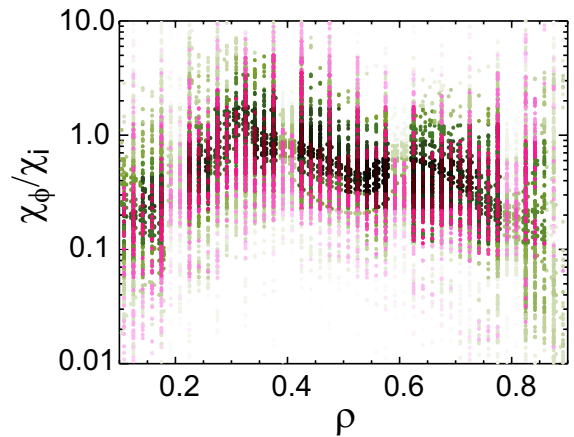


Figure 14. Profile of the Prandtl number calculated from TRANSP analysis of L-mode (green) and H-mode (magenta) discharges.

A number of quasi steady state L-mode discharges were used to investigate the global

particle transport in MAST by looking at the parameter dependence of the density peaking $\hat{n} = n_{e,0}/\langle n_e \rangle$. A strong inverse correlation of $\gamma_{j_\star \hat{n}} = -0.62$ is seen with the dimensionless, averaged current density $j_\star = \mu_0 I_p R / (S_{pl} B_t)$ on MAST ($\gamma_{xy} = (\sum x_i y_i - n \bar{x} \bar{y}) / [(n - 1) \sigma_x \sigma_y]$; σ the standard deviation, S_{pl} : area of the poloidal cross section). A slightly stronger and positive correlation of $\gamma_{\hat{n} \bar{s}} = 0.72$ is observed with $\bar{s} = q_{95}/q_0$, and a weak negative correlation with loop voltage V_{loop} . Almost no correlation is seen with ν_\star . In the \hat{n} versus j_\star space the MAST data are well aligned with TCV data from Ref. [46]. The strong correlation with j_\star and not V_{loop} suggests the presence of a turbulent pinch [47] with the Ware pinch playing a minor role.

A pinch in the core ($r/a < 0.6$) of the order of $V_Z \approx -10$ m/s is also observed for the main impurity Carbon. In Fig. 13 the profile of the ratio of pinch velocity and diffusion coefficient V_Z/D_Z for C^{6+} in a typical L-mode discharge is shown. The transport coefficient profiles are derived from modelling the measured Z_{eff} profile by solving the particle balance $\partial n_Z / \partial t = -\nabla \{-D_Z \nabla n_Z + V_Z n_Z\} + \sum_j S_{Z,j}$ ($S_{Z,j}$: source terms) using the STRAHL code [45] with a constant diffusion coefficient of $D_Z = 1$ m²/s consistent with a particle confinement time of $\tau_p \approx a^2 / (6D_Z) \approx 0.05$ s. Here, C is assumed to be the only impurity and the profiles of T_e and n_e , as well as the C influx are measured. The modelling suggests an outward convection for the impurities of order of $V_Z \approx 15$ m/s in the periphery due to a minimum in the Z_{eff} and C^{6+} profiles around $r/a \sim 0.6$. Such a minimum requires the reversal of V_Z for realistic profiles of D_Z . The low impurity peaking in the core indicates that turbulent transport or outward convection balances the neoclassical inward pinch.

5.3. Momentum confinement:

Understanding the plasma flow has become increasingly important in recent years. This is not only because of the impact on plasma confinement due to turbulence suppression by sheared flows [48, 49], which give rise to internal transport barriers (ITB), but also due to the impact of flow on MHD stability [50, 51]. Plasmas in NBI heated spherical tokamaks show a fast toroidal rotation with thermal Mach numbers measured on MAST of up to $M_{th} = v_\phi / v_{th} \lesssim 0.8$ [52]. On many tokamaks a link between momentum confinement and energy confinement has been observed [53], with the so called Prandtl number $P_\phi = \chi_\phi / \chi_i \approx 1$ relating ion momentum and ion energy diffusivity. This is consistent with theoretical studies of ITG transport. In particular in discharges with counter current NBI a substantial improvement of the confinement with plasma rotation is observed [54]. This can be readily understood by flow shear stabilisation of turbulence [48, 55], the shear on MAST being sufficient to stabilise ITG turbulence [55] (see above).

On MAST P_ϕ is also of the order unity, as can be seen from Fig. 14 [56] showing the profile of P_ϕ for various time slices in a number of L-mode (green) and H-mode (magenta) discharges calculated using the TRANSP code [57]. The data naturally have a large scatter, but clump around $P_\phi \approx 1$ for $0.1 < \rho < 0.7$ decreasing towards the edge. Even though χ_i

approaches neoclassical values, momentum transport is still dominated by turbulent processes, because for neoclassical transport $\chi_\phi^{\text{neo}} \ll \chi_i^{\text{neo}}$ (by one or two orders of magnitude). Hence, the residual turbulence contributes little to χ_i but dominates χ_ϕ . A correction of the TRANSP χ_ϕ^{eff} by a momentum pinch generated by the ‘‘Coriolis drift’’ influencing small scale instabilities [58] $\chi_\phi = \chi_\phi^{\text{eff}} [1 - (L_\omega V_\phi^{\text{pinch}})/L_n]^{-1}$ with $RV_\phi^{\text{pinch}} = -\chi_\phi (R/L_n + 4)/2$ and L_n the density gradient length, increases P_ϕ in the plasma edge, where L_n is short, leading to $P_\phi \gg 1$.

6. Fast particle instabilities:

The low toroidal field $B_t \approx 0.5$ T in beam heated STs has the consequence that the speed of the injected particles is well above the Alfvén velocity $v_A = B_t / \sqrt{(\mu_0 \sum_i n_i m_i)} \approx 1 \times 10^6$ m/s for beam energies $E_{\text{NBI}} > 30$ keV. Therefore, a wide variety of Alfvénic and fast particle driven activity is observed on MAST [59, 60].

In particular a fast particle driven $n = 1$ internal kink is observed with several harmonics at frequencies $f_{\text{LLM}} = (10 - 80)$ kHz [59]. The mode develops, as q evolves, out of $n = 1$ chirping fishbone activity. In some shots the mode couples to low frequency tearing activity in other shots it has been observed to transform back into chirping fishbone activity. During the life time of this mode a reduction of core electron and ion temperature, core rotation and core density in H-mode is observed. This can be interpreted by an increased loss of fast ions due to this mode, which is consistent with bolometer measurements sensitive to fast particle losses and TRANSP analysis showing too high a neutron rate.

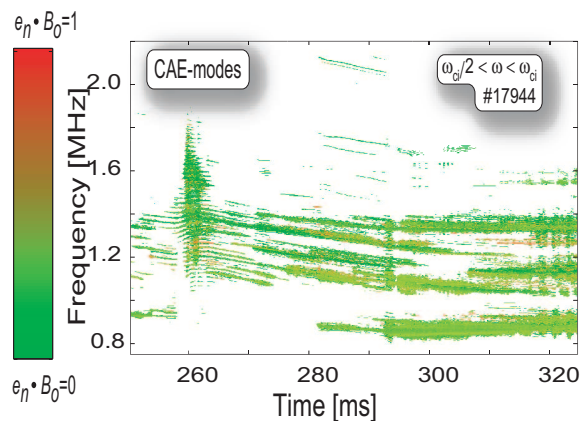


Figure 15. Polarisation of high-frequency magnetic activity showing clear elliptic polarisation with δB_{\parallel} of the order of δB_{\perp} indicative of CAE activity.

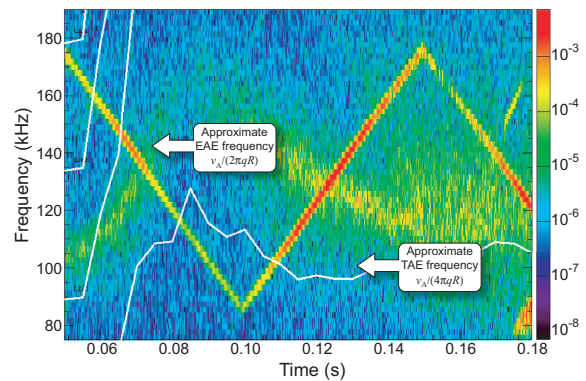


Figure 16. Frequency spectrum of LFS Mirnov coil during a TAE antenna sweep.

Magnetic activity has been observed up to $f \leq 3.8$ MHz. Modes with $f_{\text{CAE}} = (0.6 - 3.8)$ MHz have been identified as Compressional Alfvén Eigenmodes (CAE) by their elliptic polarisation with δB_{\parallel} of the order of δB_{\perp} [59, 61] (Fig. 15). An eigenmode analysis

for the measured frequencies and mode numbers, together with the resonance condition for the beam, places these modes around mid radius on the LFS. In this region $2\pi f_{\text{CAE}} \gtrsim \omega_{\text{ci}}$. CAE's have also been identified at lower frequencies around $\omega_{\text{ci}}/2$ suggesting that CAE's exist in two distinct ranges of k_{\parallel} . At lower frequency $f_{\text{TAE}} = (0.1 - 0.2)$ MHz the polarisation of toroidal Alfvén eigenmodes (TAE) has been measured showing their shear-Alfvén character.

6.1. TAE damping:

Apart from studying the unstable modes as discussed in the previous section one can also study the stable modes by actively exciting them with an antenna. For this each of the 6 lower coils of the new internal 12 coils set (Sec. 3.2) can be connected to individual 500 W power amplifiers driving a maximum current $I_{\text{int}}^{\text{AC}} \leq 4$ A with frequencies up to $f_{\text{coil}} \leq 0.5$ MHz. The 6 upper coils are then used as detection coils supplementing the extensive set of LFS Mirnov coils.

Initial experiments were started in 2007 using two of three test coils (toroidal locations: 0° , 60° , and 180°) in $n = 1$ configuration. As can be seen from Fig. 16 showing the magnetic spectrogram during an antenna sweep from 85 kHz to 180 kHz, there are two resonances at $t_1 \approx 65$ ms and $t_2 \approx 120$ ms at frequencies $f_{\text{EAE}} \approx 0.14$ MHz close to the frequency of Ellipticity-induced Alfvén Eigenmodes [62] on MAST. The detailed interpretation of these resonances is the subject of on-going theoretical and experimental work now the full set of coils is commissioned.

7. Current Drive and Start-up:

One of the major challenges for future steady state STs with high neutron flux is plasma start-up, current ramp-up and current sustainment without a high flux solenoid. Furthermore, low order rational surfaces have to be avoided by operating with $q_{\text{min}} > 1.3$, because of the detrimental impact of low n MHD such as infernal modes [50], NTMs and “monster” sawteeth [51].

7.1. EBW start-up:

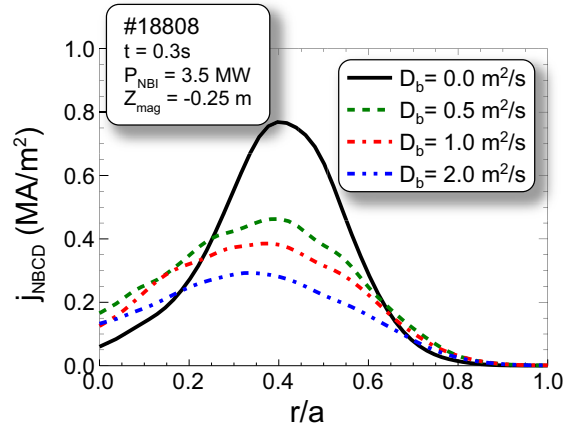
A short pulse ($\Delta t \leq 90$ ms) 100 kW $f_{\text{ECRH}} = 28$ GHz ECRH system was commissioned to study plasma start-up with EBW current drive [63]. The waves are launched in O-mode ($n_{\text{cut-off}} \approx 10^{19} \text{ m}^{-3}$) from the LFS and converted to X-mode using a grooved tile at the mid-plane of the centre column as a mirror-polariser. At the upper hybrid resonance the X-mode waves are converted into electrostatic EBW waves [64] and subsequently absorbed at the Doppler shifted electron cyclotron resonance. The waves are launched with a poloidal angle of $\alpha \approx 10^\circ$ from below the mid-plane and are absorbed above the mid-plane. With a symmetrical vertical field, B_v , following the RF break-down a pressure driven current appears near the mid-plane slowly shifting downwards as a negative EBW driven current appears above the mid-plane. These two currents repel each other and lead to a decay of the total plasma current regardless of further B_v ramp-up or RF injection. This loss of plasma current

can be prevented by either shifting the plasma initially up until closed flux surfaces (CFS) form or by applying a concave curvature to the vertical field using the divertor coils with inverted current during the initial phase of the plasma formation. Once CFS are established the plasma is shifted to the vertically stable mid-plane position or the divertor coils can be operated in their normal polarisation. Using these two techniques hot plasmas with $n_e \leq 2 \times 10^{18} \text{ m}^{-3}$ and $T_e \leq 0.7 \text{ keV}$ have been sustained for 200 ms. The pure EBW driven current is $I_p = 17 \text{ kA}$ at constant B_v . With B_v ramp-up this can be increased to $I_p = 33 \text{ kA}$, and by using less than 0.5% of the available solenoid flux ($\Psi_{\text{sol}} = 0.2 \text{ V} \times 20 \text{ ms}$) $I_p = 55 \text{ kA}$ can be sustained.

7.2. Off-axis NBCD and current ramp-up optimisation:

For future ST devices a broad current profile with $q_{\text{min}} > 1.3$ is needed to achieve high elongation with high bootstrap current and to avoid detrimental low n MHD. In order to sustain such a profile one needs off-axis current drive, since the current diffusion as well as the on axis NBI will lead to a peaked current profile in the flat-top eventually. Off-axis NBI on MAST is achieved by shifting the magnetic axis of the plasma far off the mid-plane ($\Delta Z_{\text{mag}} \lesssim 0.35 \text{ m}$) [65]. T_e , plasma energy W_{pl} , and neutron rate S_n in these extreme SN discharges ($I_p = 0.6 \text{ MA}$, $P_{\text{NBI}} = 3.5 \text{ MW}$) are comparable to similar DN discharges, although the confinement of the beam should be better in DN. This suggests either a higher energy confinement in the off-axis heated SN discharges compared to the DN discharges, or a better confinement of the off-axis beam than classical beam modeling suggests.

Figure 17. TRANSP simulations of NB driven current for various values of anomalous fast particle diffusion D_b due to fishbones.



Analysis using TRANSP suggests that about 30% of the total current is driven off-axis with the peak at $r/a \approx 0.4$ (Fig. 17). To match the measured neutron rate, S_n , and W_{pl} with TRANSP an ad-hoc anomalous fast ion diffusion of $D_b \approx 0.5 \text{ m}^2/\text{s}$ was introduced. However, the discrepancy only exists from $t_1 = 0.2 \text{ s}$ to $t_2 = 0.4 \text{ s}$, otherwise $D_b \approx 0$. During this time strong $n = 1$ fishbone activity is observed. This activity may well lead to the radial transport of fast ions [66]. The effect of the anomalous fast ion diffusion on the current profile is shown in Fig. 17. The level is comparable to values reported from DIII-D [66] and ASDEX Upgrade [67].

First measurements with the new MSE system [7] for downwards shifted, $Z_{\text{mag}} =$

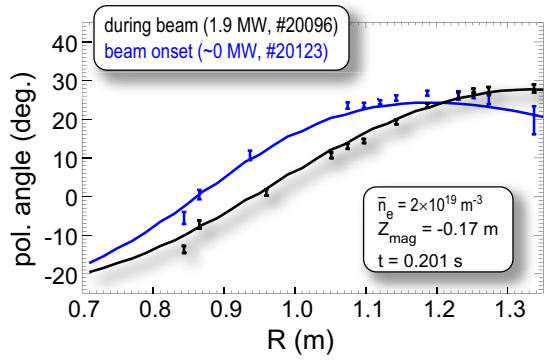


Figure 18. Comparison of measured polarisation angles from MSE at the NBI onset (blue) and well into the heating phase with $P_{\text{NBI}} = 1.9$ MW in a shifted SN plasma. The solid lines show the fit of the poloidal angle with a 1D MSE constraint in the equilibrium reconstruction.

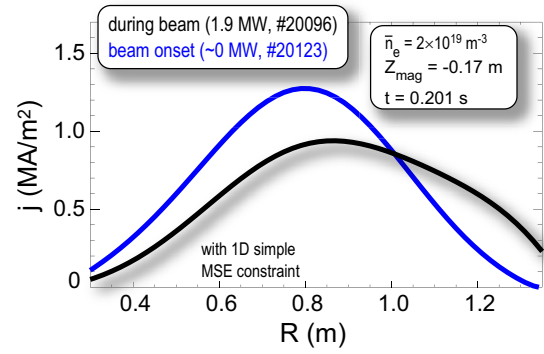


Figure 19. Comparison of current profiles derived from MSE constrained EFIT (see Fig. 18) at the NBI onset (blue) and well into the heating phase for $P_{\text{NBI}} = 1.9$ MW in a shifted SND configuration.

-0.17 m SN plasmas are shown in Fig. 18 for two discharges with a different NBI onset. Both measurements are at the same time in the discharge. The data shown in black is well into the heating phase with off-axis $P_{\text{NBI}} = 1.9$ MW and the data shown in blue are taken just at the delayed onset of the NBI in a similar discharge. It is evident that the difference in heating and possibly current drive leads to a clearly measurable difference in polarisation angle. The solid lines are the fit to the poloidal angle using the typical 1D MSE constraint in the EFIT equilibrium reconstruction. The corresponding current profiles are plotted in Fig. 19 showing a broader profile for the beam heated case. This data are consistent with off-axis NBCD, and illustrates the capability of the diagnostic. Nevertheless, validation by dedicated TRANSP modeling is on-going to evaluate the differences in $j(R)$ that may arise from the different heating schema and therefore different current profile evolution during the ramp phase alone.

In future devices non inductive current ramp up, e.g. EBWCD and NBCD will, be used to form the current profile for the steady state. The high neoclassical resistivity in an ST, however, leads to a fast current penetration, and therefore to a rapid peaking of the current profile. This may be avoided by optimising the current ramp up with respect to heating, fuelling and current ramp rate. The q -profile formation during the ramp phase was analysed using TRANSP for a set of discharges with varying density and current ramp rates, as well as different NBI ($P_{\text{NBI}} = 1.4$ MW) onset during the current ramp [68, 69]. The TRANSP runs were benchmarked against the q_{min} evolution estimated from the onset of Alfvén cascades [59] as well as the onset of other MHD. The q -profiles at the end of the current ramp were compared. Without NBI the density ramp rate has little effect on the always monotonic q -profile. With a faster current ramp the whole q -profile is elevated. Early NBI leads to a reversal of the q -profile due to off-axis ($r/a \approx 0.4 - 0.5$) pile-up of Ohmic current (the NB driven current is only 5% – 7%). This is more pronounced with the faster density ramp. The

on axis NBI heats the core reducing the resistivity, therefore increasing the current penetration time. This heating is proportional to I_p and n_e . Using this technique q-profiles with $q_{\min} > 2$ were formed approaching those foreseen in the upgraded MAST.

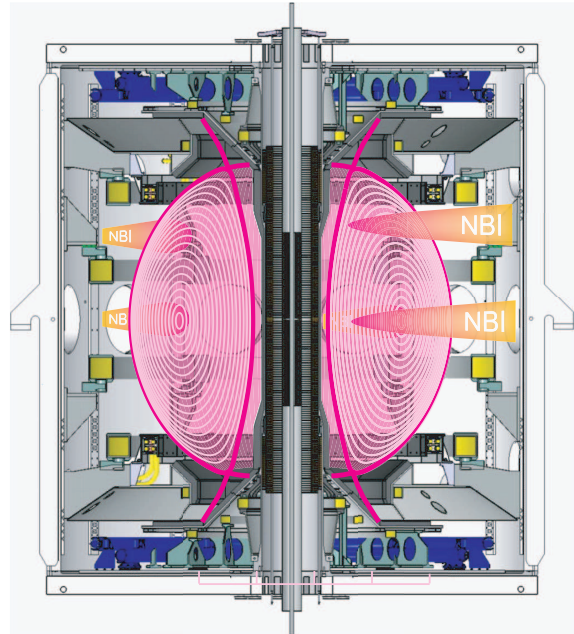
8. An upgrade to MAST

A possible future for the ST line is the prospect of realising a compact and low tritium consumption CTF without relying on tritium breeding. The main elements of the physics basis for such a device are still missing and require upgrades to existing STs. As an illustration of the type of upgrade needed we outline one being developed for MAST. Such a device would also provide strong contributions to ITER and DEMO physics in areas such as energetic particle physics, finite Larmor radius effects, model and theory testing, and physics database consolidation.

The key aim of the upgrade is to provide long pulse quasi stationary discharges with an actively driven, broad current profile to demonstrate plasma scenarios and provide a research platform. The elevated q-profile with $q_{\min} > 1.4 - 2$ needs to be sustained for flat-top times in excess of several current diffusion times, $\tau_R \approx (0.5 - 0.9)$ s. To achieve this, in particular, a flexible current drive system including off-axis current drive as well as good density control are needed. The former will be provided by up to five neutral beam injectors with $P_{\text{NBI}} = 2.5$ MW each. The beam configuration has up-to four beams injecting in co-current direction, including two off-axis beams mounted 70 cm above the mid-plane, and one on-axis beam injecting in counter current direction, allowing for extensive q-profile and rotation control. The density control will be achieved by a closed divertor with strong cryo-pumping. In Fig. 20 a current CAD configuration drawing overlaid with a typical equilibrium

Figure 20. Schematic CAD drawing of the planned upgrade to MAST overlaid with a modelled equilibrium from TRANSP for a typical discharge. The key parameters are tabulated below.

I_p	$\lesssim 2$ MA
B_t	$\lesssim 0.8$ T
Δt_{ft}	$\lesssim 5$ s
δ	0.6
κ	2.5
P_{NBI}	12.5 MW
P_{EBW}	1 MW
f_{NI}	$\lesssim 1$



from a TRANSP calculation is depicted. The outer poloidal field coils are drawn in yellow,

the load assembly structures in gray and the cryo-pumps in blue. To allow good strike point control, necessary to achieve good pumping efficiency, the present single divertor coils in the upper and lower divertor are replaced by four in-vessel coils and one HFS ex-vessel coil in each of the two divertors. The ex-vessel HFS coil also provides higher shaping capabilities. Furthermore an additional ex-vessel HFS shaping coil is added at the mid-plane.

The low density $n_e/n_G \lesssim 0.24$ together with the high heating power leads to a high fast particle fraction $\beta_{\text{fast}} = (2 - 20)\%$ dominating the free energy as in burning plasma devices. To study plasma confinement and transport in a wide operating regime the toroidal field will be increased by about 50% and the plasma current capability by a factor of two in sustained I_p . The projected performance derived from a large number of TRANSP simulations using relatively conservative assumptions such as existing kinetic profiles and H-mode confinement with $H_{\text{H98}} = \tau_E/\tau_E^{\text{IPB98}(y,2)} \approx 1$ include scenarios with 100% non-inductive current drive at $I_p = 1.2$ MA sustainable for over $5\tau_R$. Here, most of the current is neutral beam driven allowing detailed studies of NBCD physics and plasma current control without a solenoid.

Other important areas are the proof of principle test of EBW heating and current drive using a $P_{\text{EBW}} = (1 - 2)$ MW or the test of novel divertor concepts such as the extended (“super”) X-divertor [70]. Such a divertor concept may be needed for DEMO if radiative cooling of a conventional divertor proves to be too difficult, and may be crucial for a CTF. ELM suppression coils as well as a continuous pellet injector for fuelling and possibly also ELM control studies are also planned. This package of changes would make the overall device a flexible tool to address the physics needs for future tokamaks.

9. Conclusions:

Over the last two years research on MAST has made contributions to a variety of areas important not only for future spherical tokamaks (ST), but importantly also for ITER and DEMO. This is facilitated by continuous improvements to plant, diagnostics and analysis techniques. Notable contributions to ITER and DEMO physics are in the areas of pellet fuelling, ELM and pedestal physics, as well as fast particle driven instabilities. More ST specific areas include off-axis neutral beam current drive (NBCD), and electron Bernstein wave current drive (EBWCD) start-up. Many of the studies done are original to the ST. In particular shallow pellet fuelling, ELM mitigation with off mid-plane $n = 3$ coils, the active excitation of otherwise stable Alfvén eigenmodes, off-axis NBCD, and EBWCD start-up are unique in the ST. Here, a possible design limitation in the original ITER design with respect to particle throughput was explored. The frequency of ELMs was increased with $n = 2$ resonant magnetic perturbations using external coils. 30% off-axis current was driven with $P_{\text{NBI}} = 3.5$ MW, and plasma start-up with EBWCD was demonstrated ($I_p = 55$ kA with 0.5% solenoid swing and $P_{\text{RF}} = 0.1$ MW). In order to model MAST plasmas adequately turbulence, predictive transport and MHD codes are continually improved by the requirements to include strong flow shear, finite pressure β (electromagnetic effects), and finite Larmor radius physics. For example the new TGLF reduced transport model is tested using MAST discharges giving reasonable agreement, but only if $E \times B$ flow shear

is included. The different energy confinement scaling for the ST with weaker $I_p^{0.6}$ and stronger $B_t^{1.4}$ dependence than the IPB98(y,2) scaling may already emphasise the differences expected in future high β regimes and could lead to a different design optimisation for an ST-CTF. The near isotropic fast particle distribution at the resonant Alfvén velocity mimics burning plasmas and Alfvénic activity with elliptic polarisation is observed with frequencies up to $f = 3.8$ MHz of the order of the ion cyclotron frequency. The fast particle driven activity is already seen to affect neutral beam heating, current drive and torque. Challenging measurements like the structure of the edge radial electric field with resolution better than the ion Larmor radius, the q-profile (motional Stark effect) at low magnetic field, and the local density fluctuations (beam emission spectroscopy) allow new physics to be investigated such as the interplay between pressure gradient and electric field gradient. The characterisation of the dynamics of inter-ELM and L-mode filaments will guide the interpretation of scrape-off layer transport. The research also consolidates the physics basis of an upgrade to MAST, designed to study current drive and fast particle physics, as well as divertor power handling and pumping in long pulses with a relaxed current profile.

Acknowledgements: This work was jointly funded by the UK Engineering and Physical Sciences Research Council and by the European communities under the Contract of Association between EURATOM and UKAEA. The views and opinions expressed herein do not necessarily reflect those of the European Commission. NBI equipment is on loan from ORNL, the NPA from PPPL and the pellet injector was provided by FOM. Plasma control software was provided by GA.

References

- [1] DARKE, A., HARBAR, J. R., HAY, J. H., et al., MAST: A mega amp spherical tokamak, in *Proceedings of the 18th Symposium on Fusion Technology*, 1994.
- [2] ITER-TEAM, *ITER Physics Basis*, volume 39, chapter 2, pp. 2175–2249, Nucl. Fusion, 1999.
- [3] IKEDA, K. et al., Nucl. Fusion **47** (2007) S1.
- [4] VOSS, G., DAVIS, S., DNESTROVSKIJ, A., et al., Fusion Eng. and Design (2008), in press.
- [5] WILSON, H., AHN, J.-W., AKERS, R., et al., Nucl. Fusion **44** (2004) 917.
- [6] KULDKEPP, M., WALSH, M. J., CAROLAN, P. G., et al., Rev. Sci. Instr. **77** (2006) 10E905.
- [7] BOCK, M. F. M. D., CONWAY, N. J., WALSH, M. J., CAROLAN, P. G., and HAWKES, N. C., Rev. Sci. Instr. **79** (2008) 10F524, PROCEEDINGS OF THE 17TH TOPICAL CONFERENCE ON HIGH-TEMPERATURE PLASMA DIAGNOSTICS (HTPD0).
- [8] SCANNELL, R., WALSH, M. J., CAROLAN, P. G., et al., Rev. Sci. Instr. **79** (2008) 10E730, PROCEEDINGS OF THE 17TH TOPICAL CONFERENCE ON HIGH-TEMPERATURE PLASMA DIAGNOSTICS (HTPD0).
- [9] MEYER, H., BUNTING, C., CAROLAN, P. G., et al., Journ. Phys.: Conf. Series **123** (2008) 012005.
- [10] SCANNELL, R., WALSH, M. J., CAROLAN, P. G., et al., Rev. Sci. Instr. **77** (2006) 10E510.
- [11] KIRK, A., COUNSELL, G. F., ARENDS, E., et al., Plasma Phys. Control. Fusion **46** (2004) A187.
- [12] MEYER, H., CAROLAN, P. G., CONWAY, G. D., et al., Nucl. Fusion **46** (2006) 64.
- [13] KIRK, A. et al., H-mode pedestal characteristics on MAST, submitted to Plasma Phys. Contr. Fusion.
- [14] MEYER, H., CAROLAN, P. G., CONWAY, N. J., et al., Plasma Phys. Control. Fusion **47** (2005) 843.
- [15] MAINGI, R., HUBBARD, A., MEYER, H., et al., Comparison of small ELM characteristics and regimes in Alcator C-MOD, MAST, and NSTX, in *Proc. 22nd IAEA FEC*, 2008.
- [16] MAINGI, R., BUSH, C. E., FREDRICKSON, E. D., et al., Nucl. Fusion **45** (2005) 1066.
- [17] WILSON, H. R., SNYDER, P. B., HUYSMANS, G. T. A., and MILLER, R. L., Phys. of Plasmas **9** (2002) 1277.

- [18] SNYDER, P. B. et al., Pedestal Stability Comparison and ITER Pedestal Prediction, in *Proc. 22nd IAEA FEC*, 2008, to be submitted to Nucl. Fusion.
- [19] URANO, H., TAKIZUKA, T., KAMADA, Y., et al., Nucl. Fusion **48** (2008) 045008 (9pp).
- [20] EVANS, T., MOYER, R., BURRELL, K., et al., Nature Physics **2** (2006) 419.
- [21] KIRK, A. et al., ELM power loadings and control on MAST using resonant magnetic perturbations, in *Proc. 22nd IAEA FEC*, 2008, to be submitted to Nucl. Fusion.
- [22] LIANG, Y., KOSLOWSKI, H., THOMAS, P., et al., Phys. Rev. Lett. **98** (2007) 265004.
- [23] CHIRIKOV, B. V., Journal of Nuclear Energy. Part C, Plasma Physics, Accelerators, Thermonuclear Research **1** (1960) 253.
- [24] NARDON, E. et al., Journ. Nucl. Mat. (2008), to be published, preprint available.
- [25] HOWELL, D. F., HENDER, T. C., and CUNNINGHAM, G., Nucl. Fusion **47** (2007) 1336.
- [26] COLTON, A., BUTTERY, R., FIELDING, S., et al., Nucl. Fusion **39** (1999) 551.
- [27] FIELDING, S., BUTTERY, R., FIELD, A., et al., ELM control in COMPASS-D, in *Proc. 28th EPS Conf. Control. Fusion and Plasma Phys.*, pp. 1825–1828, 2001.
- [28] VALOVIC, M., AXON, K., GARZOTTI, L., et al., Nucl. Fusion **48** (2008) 075006 (8pp).
- [29] VALOVIC, M. et al., Confinement and fuelling in MAST, in *Proc. 22nd IAEA FEC*, 2008.
- [30] KOTSCHENREUTHER, M., REWOLDT, G., and TANG, W., Comp. Phys. Comm. **88** (1995) 128.
- [31] THYAGARAJA, A., KNIGHT, P. J., DE BAAR, M. R., HOGEWELJ, G. M. D., and MIN, E., Phys. of Plasmas **12** (2005) 090907.
- [32] KIRK, A., WILSON, H. R., COUNSELL, G. F., et al., Phys. Rev. Lett. **92** (2004) 245002.
- [33] KIRK, A., COUNSELL, G. F., WILSON, H. R., et al., Plasma Phys. Control. Fusion **46** (2004) 551.
- [34] ZOHN, H., Plasma Phys. Control. Fusion **38** (1996) 105.
- [35] GOODALL, D., Journ. Nucl. Mat. **111** (1982) 11.
- [36] ZWEBEN, S. J., MCCHESNY, J., and GOULD, R. W., Nucl. Fusion **23** (1983) 825.
- [37] BEN AYED, N., KIRK, A., DUDSON, B., et al., Experimental observation of inter-ELM filaments on MAST, in *Proc. 35th EPS Plasma Physics Conference*, 2008, submitted to Plasm. Phys. Contr. Fusion.
- [38] DUDSON, B. D., AYED, N. B., KIRK, A., et al., Plasma Phys. Control. Fusion **50** (2008) 124012 (9pp).
- [39] XU, X. Q., COHEN, R. H., PORTER, G. D., et al., Nucl. Fusion **40** (2000) 731.
- [40] LISGO, S. et al., The Influence of Filaments on Scrape-Off Layer Transport, in *Proc. 22nd IAEA FEC*, 2008, to be submitted to Nucl. Fusion.
- [41] AKERS, R. et al., Transport studies in the MAST spherical tokamak, in *Proc. 22nd IAEA FEC*, 2008, to be submitted to Nucl. Fusion.
- [42] STAEBLER, G. M. et al., Testing the Trapped Gyro-Landau Fluid Transport Model with Data from Tokamaks and Spherical Tori, in *Proc. 22nd IAEA FEC*, 2008.
- [43] DNESTROVSKIJ, A. et al., Canonical Profiles Transport Model for H-mode shots in Tokamaks, in *Proc. 22nd IAEA FEC*, 2008.
- [44] KAYE, S., BELL, M., BELL, R., et al., Nucl. Fusion **46** (2006) 848.
- [45] BEHRINGER, K., R (87) **8** (1987).
- [46] ZABOLOTSKY, A., WEISEN, H., and TEAM, T., Plasma Phys. Control. Fusion **45** (2003) 735.
- [47] GARBET, X., GARZOTTI, L., MANTICA, P., et al., Phys. Rev. Lett. **91** (2003) 035001.
- [48] TERRY, P. W., Rev. Mod. Phys. **72** (2000) 109.
- [49] WOLF, R. C., Plasma Phys. Control. Fusion **45** (2003) R1.
- [50] MENARD, J. E. et al., Nucl. Fusion **43** (2003) 330.
- [51] CHAPMAN, I. T., PINCHES, S. D., GRAVES, J. P., et al., Plasma Phys. Control. Fusion **49** (2007) B385.
- [52] AKERS, R. J. et al., Plasma Phys. Control. Fusion **45** (2003) A175.
- [53] TALA, T., CROMBÉ, K., DE VRIES, P. C., et al., Plasma Phys. Control. Fusion **49** (2007) B291.
- [54] COUNSELL, G., AKERS, R., APPEL, L., et al., Nucl. Fusion **45** (2005) S157.
- [55] FIELD, A., AKERS, R., APPLGATE, D., et al., Core Heat Transport in the MAST Spherical Tokamak, in *Proc. 20th IAEA Fusion Energy Conf. on Fusion Energy 2004 (Vilamoura, 2004)*, 2004.
- [56] FIELD, A. R., AKERS, R. J., CONWAY, N. J., et al., Momentum transport in MAST spherical tokamak plasmas, in *Proc. 35th EPS Plasma Physics Conference*, 2008, to be published in Plasm. Phys. Contr.

Fusion.

- [57] HAWRYLUK, R. J., An empirical approach to tokamak transport, in COPPI, B. et al., editors, *Physics of plasmas close to thermonuclear conditions*, volume 1, CEC, Brussels, 1980.
- [58] PEETERS, A. G., ANGIONI, C., and STRINTZI, D., Phys. Rev. Lett. **98** (2007) 265003.
- [59] GRYAZNEVICH, M., SHARAPOV, S., LILLEY, M., et al., Nucl. Fusion **48** (2008) 084003.
- [60] PINCHES, S. et al., Fast particle instabilities in MAST, in *Proc. 22nd IAEA FEC*, 2008, to be submitted to Nucl. Fusion.
- [61] APPEL, L. C., FÜLLOP, T., HOLE, M. J., et al., Plasma Phys. Control. Fusion (2008), accepted.
- [62] BETTI, R. and FREIDBERG, J. P., Physics of Fluids B: Plasma Physics **4** (1992) 1465.
- [63] SHEVCHENKO, V., BARANOV, Y., O'BRIEN, M., and SAVELIEV, A., Phys. Rev. Lett. **89** (2002) 265005.
- [64] LAQUA, H. P., Plasma Phys. Control. Fusion **49** (2007) R1.
- [65] LLOYD, B. et al., Nucl. Fusion **47** (2007) S658.
- [66] HEIDBRINK, W. W. et al., Nucl. Fusion **42** (2002) 972.
- [67] GÜNTER, S. et al., Nucl. Fusion **44** (2005) S98.
- [68] KEELING, D., AKERS, R., CHALLIS, C. D., CUNNINGHAM, G., and MEYER, H., Tailoring the q-profile on MAST for scenario optimisation, in *Proc. 35th EPS Plasma Physics Conference*, 2008.
- [69] TURNYANSKIY, M. R., KEELING, D., AKERS, R. J., et al., Current profile control studies on MAST, in *Proc. 22nd IAEA FEC*, 2008.
- [70] KOTSCHENREUTHER, M., VALANJU, P. M., MAHAJAN, S. M., and WILEY, J. C., Phys. of Plasmas **14** (2007) 072502.